ADVANCED MATERIALS TECHNOLOGIES
www.advmattechnol.de

A Paraffin-Based Photoresin: 3D Printing of Paraffin for Encapsulation-Free Shape-Stabilized Paraffin-Based Phase Change Materials

Swathi Krishna Subhash, Qingchuan Song, Paul H. Kamm, Santiago Franco, Yunong Chen, Dorothea Helmer, Uwe Pelz, Frederik Kotz-Helmer, Peter Woias, and Bastian E. Rapp*

High-resolution structuring of paraffin wax as phase change material is essential for miniaturized applications in thermal actuators, flexible electronics, and sensors, yet requires complex encapsulation methods that limit design freedom and increase costs. A low-cost encapsulation-free approach is demonstrated for preparing shape-stabilized paraffin-based phase change materials using digital light processing based 3D printing. In this work, a paraffin-loaded photoresin with paraffin concentrations up to 60 wt.% in acrylated polymer networks. The printed parts are thermally responsive undergoing a shape-stabilized phase change, and exhibits elastic and stretchable properties. Despite the high paraffin loading, the printed parts can be stretched up to 130% in length. Differential scanning calorimetry results show that the highest phase change latent heat of the printed parts can reach 120 J · g^{-1}. Cyclic scanning differential calorimetry results show a slight shift in endothermic and exothermic signals indicating no obvious paraffin leakage. Considering that the phase transition of the paraffin in the photoresin at the melting point of paraffin affects the mechanical modulus of the printed parts, a pneumatic actuator is also printed that responds to body temperature. This work contributes a significant step toward a wide range of applications from micro sensors to new interactive soft actuators.

1. Introduction

Phase change materials (PCMs) can absorb or release latent heat[1] to buffer temperature fluctuations[2] around a constant temperature.[3] Over the last decades, PCMs have become a key component in thermal energy storage and management techniques to reduce energy consumption[4] in the heating[5] and power generation industry.[6] Paraffin wax is a widely used PCM due to its advantageous properties, such as decent latent heat (150–200 kJ kg^{-1}),[7] low corrosiveness,[8] and its lower degree of supercooling available in different transition temperatures closer to room temperature. These characteristics make paraffin ideal for thermal energy storage and management applications, especially in areas requiring temperature regulation such as building interiors,[9,10] public transport,[11,12] agriculture[13] and

S. K. Subhash, U. Pelz, P. Woias
Laboratory for Design of Microsystems
Department of Microsystems Engineering (IMTEK)
Georges-Köhler-Allee 102, 79110 Freiburg, Germany

S. K. Subhash, Q. Song, S. Franco, U. Pelz, P. Woias, B. E. Rapp
Cluster of Excellence livMatS @ FIT – Freiburg Center for Interactive Materials and Bioinspired Technologies
University of Freiburg
Georges-Köhler-Allee 105, 79110 Freiburg, Germany

S. K. Subhash, Q. Song, S. Franco, D. Helmer, U. Pelz, F. Kotz-Helmer, P. Woias, B. E. Rapp
FIT Freiburg Center of Interactive Materials and Bioinspired Technologies
University of Freiburg
Germany

Q. Song, S. Franco, Y. Chen, D. Helmer, F. Kotz-Helmer, B. E. Rapp
Laboratory of Process Technology
NeptunLab
Department of Microsystems Engineering (IMTEK)
Georges-Köhler-Allee 103, 79110 Freiburg, Germany
E-mail: frederik.kotz-helmer@neptunlab.org

P. H. Kamm
Department Microstructure and Residual Stress Analysis
Helmholtz-Zentrum Berlin für Materialien und Energie
Hahn-Meitner-Platz 1, 14109 Berlin, Germany

P. H. Kamm
Institute of Materials Science and Technology
Technische Universität Berlin
Hardenbergstr. 36, 10623 Berlin, Germany

D. Helmer, B. E. Rapp
Freiburg Materials Research Center (FMF)
University of Freiburg
79104 Freiburg, Germany

The ORCID identification number(s) for the author(s) of this article can be found under https://doi.org/10.1002/admt.202500617

DOI: 10.1002/admt.202500617

in microelectronics.[14] Recently, they have also emerged as potential candidates for functional metamaterials in, e.g., paraffin actuators, taking advantage of their inherent volume expansion during phase change.[15] Paraffin undergoes solid-liquid phase transition during heating accompanied by a substantial volume increase and decrease, respectively. Leakage is also a significant issue in these cases as it can compromise the effectiveness and reliability of the thermal management system. This requires rigid containers[16] for keeping the volume increase at bay and still can lead to leakage due to the extremely large expansion force of the solid-to-liquid phase transition. To address this issue and to reduce additional thermal resistance from the metal containers, researchers have explored shape-stabilized, container-free paraffin wax-based PCMs. Several shape-stabilizing approaches have been reported including microencapsulation with pre-made core-shell,[2] porous support[17] and polymer matrices.[18] Although core-shell encapsulated PCMs have been widely adopted, their drawbacks cannot be ignored, including additional processing costs and the negative impact of the shell material on thermal energy storage density.[19] Moreover, current stabilization methods struggle to achieve precise and continuous structures, like those required for applications like high-energy battery thermostats.[20]

Additive manufacturing (AM), commonly referred to as 3D printing, presents a novel paradigm for quickly producing precise and continuous geometries. Today, this is a widely accessible and commercially available technology for a broad range of applications.[21] Among these multitude of 3D printing technologies, digital light processing (DLP), a resin-based method which creates the designed specific structure using UV-polymerization of liquid polymer monomers and crosslinkers and allowing for high resolution and short fabrication durations.[22] According to Er et al.'s research, using DLP technology, it is possible to directly manufacture PCM structures that are encapsulated by polymer networks rather than core-shell, which effectively prevents PCM leakage while maintaining high thermal energy storage capacity, as demonstrated by their achievement of 83.7 J/g latent heat enthalpy in 50% PCM-loaded composites with homogeneous internal structure.[19] Ma et al. proposed a novel method using DLP-based 3D printing to fabricate recyclable PCM-polysiloxane networks with adjustable thermal properties, avoiding core-shell encapsulation while achieving high latent heat capacity and shape stability through polymer network self-confinement, albeit with features resolution well above the millimeter regime,[23] yet existing work has not demonstrated the ability to perform high-resolution 3D printing. Aside from the restriction on resolution, the printed PCM materials exhibit limited stretchability, which restricts their applications to rather stiff systems.

This study presents a facile approach for producing a core-shell free paraffin/elastomer composite using DLP in form of a Paraffin Photoresin, consisting of up to 60 wt.% of paraffin in a polymerizable acrylic blender. This approach is an alternative to classical paraffin containments like rigid containers and allows the per-design structuring of paraffin-loaded polymer matrices. The as-prepared structures are shape-stable continuous networks and possess thermal responsiveness. Several examinations were conducted to characterize the properties of 3D printed parts. In terms of mechanical properties, tensile tests revealed elongation ranges of 130 – 600% across different paraffin mass percentages at temperatures above paraffin's melting point, demonstrating excellent shape retention capabilities of the shape stabilized paraffin. This combination of high stretchability while maintaining latent heat represents a key advantage of this work compared to previous studies, as demonstrated in Figure S1 (Supporting Information). In terms of thermal properties, we studied differential scanning calorimetry (DSC) of the printed materials under different paraffin loadings, wherein the sample with 60 wt.% paraffin exhibited a latent heat of melting of 120 $J \cdot g^{-1}$, which is similar to other reported 3D printed PCM material based-on microencapsulation.[2] We further characterized paraffin distribution within polymer networks using micro computed Tomography (μ-CT) and Scanning Electron Microscope imaging (SEM). X-ray Diffraction (XRD) and in situ Wide-angle X-ray Scattering (WAXS) analyses revealed the material's crystallization kinetics during cooling process from 65 °C to room temperature, providing insights into its phase change dynamics. To demonstrate practical applications, we tested a 3D printed micro-house model in a heating oven to evaluate its thermal management capabilities. Additionally, we developed a body temperature-responsive pneumatic actuator that leverages the material's modulus changes during phase transitions, showcasing its potential for temperature-triggered actuator systems.

2. Results and Discussion

We formulated the Photoresin using isobornyl acrylate (IA) monomer, aliphatic urethane acrylate (AUA, Genomer 4230) crosslinker, photoinitiator (diphenyl(2,4,6-trimethylbenzoyl) phosphine oxide, TPO) and absorber (Tinuvin-326). A bio-based paraffin (CrodaTherm 37-SO-(GD)) was incorporated into the formulation at concentrations ranging from 20 to 60 wt.%. The samples are denoted as PA X, where X represents the weight percentage of paraffin (e.g., PA 20 for 20 wt.%). A reference sample without paraffin was prepared and denoted as PA 00, as shown in **Figure 1**a. Figure 1b shows a complex Kelvin foam structure yield from DLP printed Paraffin Photoresin PA 50, indicating that the polymer networks formed by the monomer and crosslinker we selected can reliably support higher concentrations of paraffin. Figure 1c shows the microstructures that can be obtained using PA 50 and a DLP with a horizontal resolution of 50 μm. One can see that the resin allows for fabrication with high resolution, which makes it potential for applications requiring microstructures of PCMs (with 58 μm of feature size≈one pixel size). This can be attributed to the low viscosity of the resins. The rheological analysis of different formulations (Figure S2, Supporting Information) shows that all PA formulations maintain suitable low viscosity for printing at 40 °C, while exhibiting sharp viscosity increases during cooling at their respective crystallization temperatures, with higher paraffin content leading to crystallization at higher temperatures. The molecular compatibility between polymer network and paraffin originates from their similar hydrocarbon-based structures, enabling homogeneous mixing above melting temperature. The compatibility between paraffin and photocurable components was also confirmed by the formation of a homogeneous, clear liquid phase at 42 °C, as demonstrated for PA 60 (Figure S3, Supporting Information), indicating successful incorporation of paraffin into the Photoresin system through ultrasonic blending.

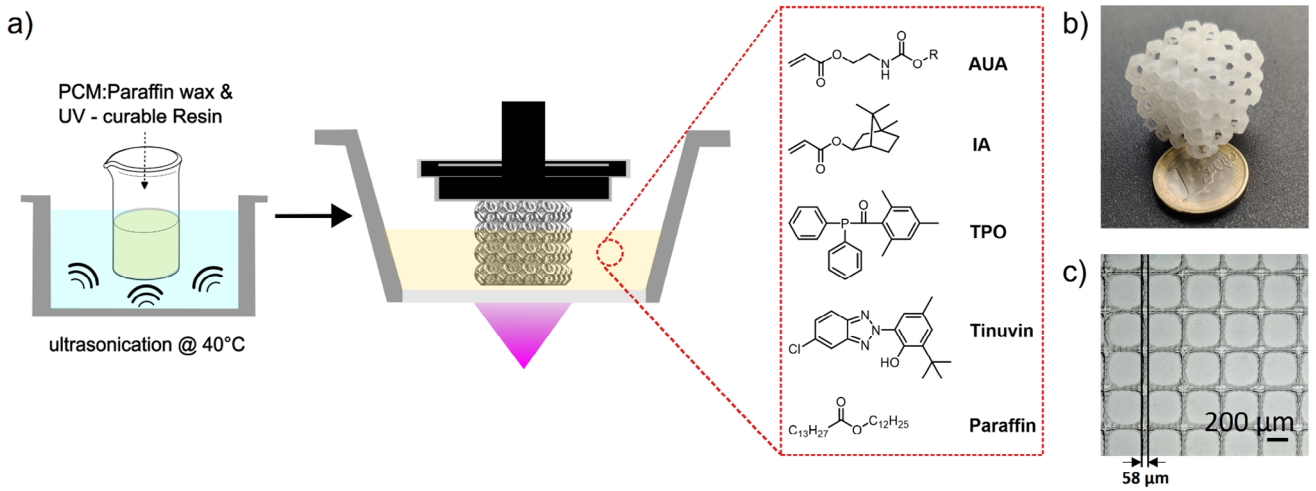

Figure 1. Formulation of the Paraffin Photoresin. a) Preparation of the Paraffin Photoresin via ultrasonication to form a uniform printable ink from paraffin, the monomer isobornyl acrylate, an aliphatic urethane acrylate crosslinker, the photoinitiator TPO and Tinuvin-326 as the UV-absorber, as well as CrodaTherm 37 paraffin. b) Example of a printed open-cell Kelvin foam at room temperature made from PA 50. c) DLP printed microstructure of the Paraffin Photoresin, showing a resolution of roughly 60 µm.

We printed a series of dogbone-shaped specimens with PA 20 to PA 60 (in increments of 10 wt.%) and the control formulation PA 00. **Figure** 2a shows the components after printing at room temperature. As can be seen, all Paraffin Photoresins could be successfully printed. The structures obtained show shape-stability and no paraffin leakage was observed physically. The printed components were soft and transparent during printing, which was conducted at 40 °C maintained by 50 °C heating airflow, and became stiff and opaque after cooling to room temperature as the paraffin solidified forming crystalline phases within the host polymer networks. In contrast to this, the sample made from the control resin PA 00 did not show any difference in transparency due to the absence of paraffin. The change in transparency is reversible, i.e., when heated above their melting point of ≈40 C, the components became transparent again as the paraffin phase-transitioned and thus the crystalline characteristics of the components disappeared. Conversely, if a sample containing paraffin is cooled below the phase transition temperature of paraffin after being heated, it will also lose transparency. Taking PA 60 as an example, as shown in Figure S4 (Supporting Information), its transmission across the UV–vis spectrum progressively decreases during the crystallization of paraffin within the polymer networks. At the same time, these materials did not undergo significant deformation before and after the phase change. The dimensional stability during phase transition was quantitatively evaluated through microscopic measurements, showing that all formulations maintain more than 98% of their original length during phase change (Figure S5, Supporting Information), indicating effective constraint of paraffin volume change by the polymer networks. To quantitatively analyze the effect of paraffin content on its mechanical properties, tensile tests were performed to characterize the mechanical stability of paraffin loaded resins (PA 20 to PA 60 at 42 °C) (see Figure 2b). The results demonstrate that with increasing paraffin mass loading, the material's maximum strain at breakage decreases from 600% for PA 20

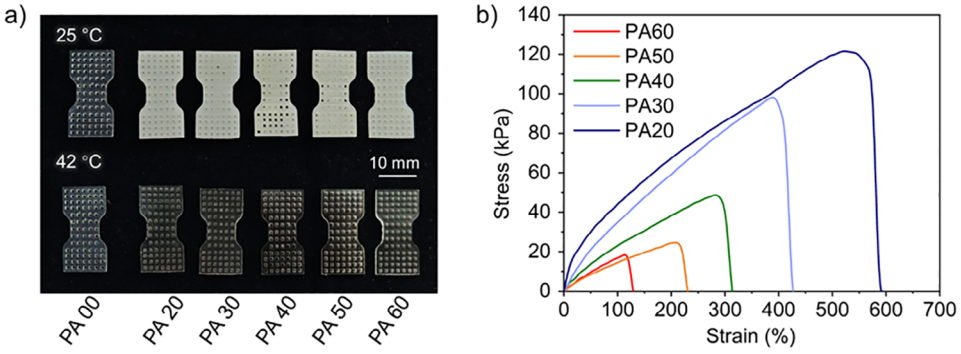

Figure 2. Printed components made from PA 20 to PA 60 in 10 wt.% increments with PA 00 serving as the control formulation. a) 3D printed dogbone-shaped structures for each formulation displaying the characteristic white hue due to the crystalline paraffin phase at 25 °C and the transparent state (due to the melting of paraffin) at 42 °C. b) Result of tensile tests on dogbone structures at 42 °C. As can be seen, the increase concentration of paraffin reduces the Young's modulus and yield strain.

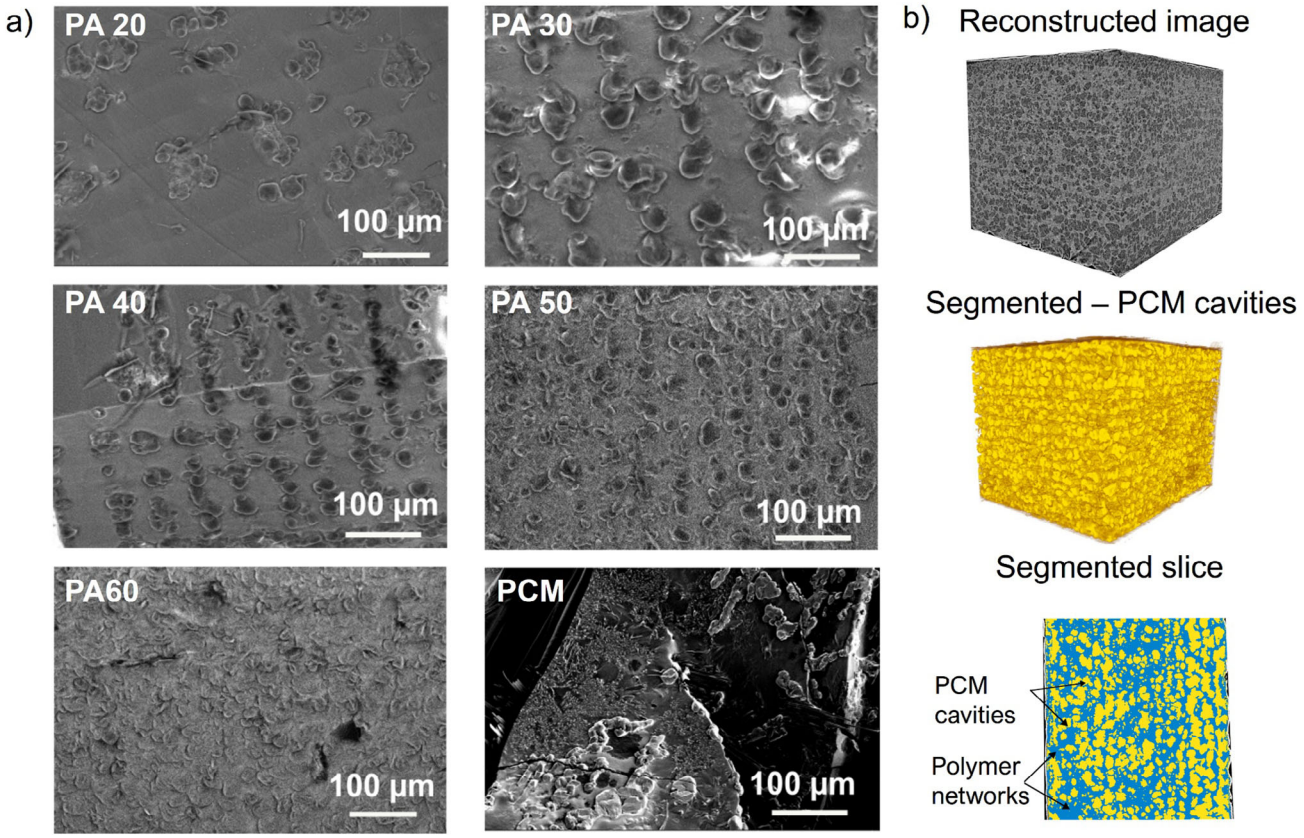

Figure 3. Morphology and structural analysis: a) SEM images of printed cured samples PA 20 to PA 50 samples (in increment of 10 wt.%) with PA 00 serving as the control. As can be seen, there is strong microphase separation of paraffin in the resin matrix thereby consistently entrapping the paraffin particles. The volumetric ratio increases with the overall increase in mass ratio. b) µ-CT analysis showing a 3D reconstruction, highlighting the paraffin entrapments. A single slice view shows matrix and paraffin part as two distinct colored regions (resin matrix: blue; paraffin: yellow).

to ≈150% for PA 60 (see Figure S6, Supporting Information for statistical analysis of strain at breakage). Figure S7 (Supporting Information) shows Young's moduli for samples PA 00 to PA 60 at both 20 and 40 °C, which indicates that PA 60 remains relatively flexible after heating even though the mechanical resilience of the material is significantly lower compared to Paraffin Photoresins with lower paraffin content. In contrast, PA 00 showed minimal change in modulus with increase in temperature, behaving as a rigid material.

Investigating the microstructure of the material and understanding the incorporation of paraffin within the polymer network will elucidate the reasons behind the non-leakage of paraffin in shape-stabilized PCMs. To further examine the microscopic morphology of the 3D printed paraffin resins, we conducted SEM analysis on five samples: PA 20, PA 30, PA 40, PA 50, and PA 60 along with pure paraffin and PA 00 (see **Figure 3**; Figure S8, Supporting Information). As can be seen, the samples have two visibly different regions: a darker region which corresponds to the paraffin microphase and a brighter region which represents the polymer matrix. The paraffin phase appears darker due to the lower electron density of paraffin (being comprised of pure hydrocarbons) in SEM. In Figure S8 (Supporting Information) the SEM image of PA 00 is displayed, which can be considered as the brighter region resin polymer matrix. The comparison of the SEM images of PA 20 to PA 50 shows that the paraffin exists as phase-separated microparticles in the polymer matrix after crystallization, which gives rise to the material opacity after cooling due to the increase in light scattering. The polymer matrix thus acts as a binder for the paraffin containing it within small particles which prevents paraffin leakage from the material.

The internal microstructure of printed PA 50 was analyzed using µ-CT. CT scans allow for analyzing the spatial distribution of paraffin within the resin matrix and thus the reconstruction of the 3D structure and can clarify the distribution of paraffin in polymer networks more directly. As stated, the resin matrix consists of heavier atoms and thus absorbs X-rays better resulting in a brighter region compared to paraffin which forms the darker regions of the CT scans. Paraffin can be observed as numerous paraffin microcavities in the range of 20–250 µm in diameter (Figure 3a). Single-slice segmentation reveals that the polymer matrix forms a continuous structure which effectively entraps or encapsulates the paraffin, resulting in the lack of paraffin leakage (Figure 3b). A slice-by-slice inspection shows visible printing layers with no crack lines, indicating that layers have merged well, which supports the reported good mechanical strength (see Video S1, Supporting Information). To study the stability of this entrapment over multiple heating and cooling cycles, we investigated the microstructure of a sample printed from PA 50 after

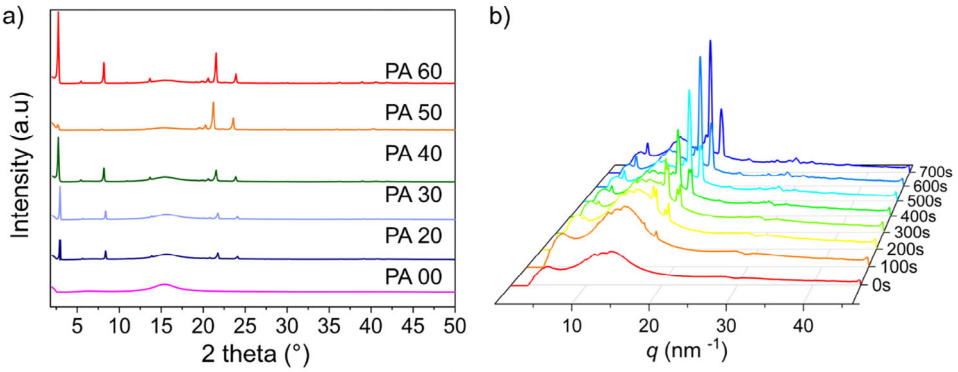

Figure 4. Assessment of the crystallinity of cured samples. a) XRD plot of printed samples of PA 00 to PA 60, with PA 00 serving as control and thus only displaying the amorphous phase of the resin. Samples PA 20 to PA 60 show definite crystalline peaks from the entrapped solid paraffin. b) Time-dependent radial integral profiles from in situ WAXS, monitoring the PA 50 crystallization process during cooling from 65 to 25 °C.

multiple melting and cooling cycles (30 times). According to the µ-CT measurement results after melting-cooling cycles in Video S2 (Supporting Information), one can see the redistribution yet non-spillover of the paraffin micro cavities, reflecting the reliability of the material as recyclable PCM.

The phase composition and degree of crystallinity of the 3D printed paraffin resins were investigated using XRD (**Figure** 4a) to examine whether the paraffin still forms crystals in the polymer network, namely the phase transition mechanism of Paraffin Photoresin. The cured paraffin-free Photoresin PA 00 showed a broad peak at $2\theta = 15°$ revealing the amorphous nature, while the cured PA 20, PA 30, PA 40, PA 50, and PA 60 all showed a crystalline peak at 21° and 24° corresponding to the 110 and 200 crystal planes of paraffin respectively,[24] along with other minor peaks. The resin's diffraction pattern shows the broad peak from the resin along with crystalline peaks from paraffin confirming the physical combination of resin and paraffin. The increased intensity of the major sharp peaks resulting from paraffin in the PA 20 to PA 60 samples is in accordance with the increase in paraffin concentration. In order to observe how quickly the crystals form, which corresponds to the speed of phase change, the crystal formation rate of PA 50 at room temperature (25 °C) from 65 °C was characterized with in situ WAXS[25] and the time-dependent radial integration profiles of cooling from 65 to 25° C are shown in Figure 4b. Figure S9 (Supporting Information) shows the ratio of change of the crystallization peak area to the total area below the curve after deducting of the baseline over time. After 700 s the crystallization was nearing completion. This result shows that the melted paraffin molecules exist in a homogeneous phase with the polymer network before cooling, which is consistent with the previous observation that it is transparent at high temperatures. Also, swelling tests (Figure S10, Supporting Information) could confirm the molecular interactions between the polymer network and paraffin. While crystallization induces phase separation below melting point, the molecular compatibility enables molten paraffin to reintegrate into the polymer network, forming a homogeneous gel above melting temperature.

The transition temperature and latent heat of phase change characterize the temperature range of operation and energy storage efficiency, which are the key properties of phase change materials. **Figure** 5a,b presents the DSC curves of uncured resin and printed parts compared to reference PA 00 and paraffin, from which the transition temperature and latent heat of printed samples were calculated (see **Table** 1). For PA 00, pure resin no phase-change peak was found, while the resins from PA 20 to PA 60 showed a phase-change between 30 and 40 °C, which corresponds to the phase-change of paraffin component at around 37 °C. DSC thermograms of pure paraffin exhibit two characteristic endothermic and exothermic peaks at Tm = 37 °C, corresponding to solid-to-liquid and liquid-to-solid phase transitions, respectively. A minor thermal hysteresis is observed between the melting and crystallization processes. When comparing uncured and cured resins, the cured resin shows similar behavior in temperature and total heat flow resulting from the paraffin-induced phase change. This suggests that the presence of polymeric networks does not significantly impact the phase change of the paraffin. The values for ΔH_m and ΔH_c, i.e., the latent heat of melting and crystallization, respectively, are derived from the DSC curve by integrating the phase change peaks (see Table 1 and Figure 5c). The increase in latent heat increases with the total amount of the paraffin. Compared to pure paraffin (208 and 206.8 $J \cdot g^{-1}$ for ΔH_m and ΔH_c respectively), the PA 60 composite – as expected – showed a reduced latent heat content of around 60% (128 and 121.3 $J \cdot g^{-1}$ respectively), corresponding to the sample composition. Since the DSC results evaluate the changes in the thermal properties depending on the amount of the paraffin in each formulation, it confirms that the absorption and release of thermal energy during melting and crystallization is solely dominated by the paraffin without being affected by polymerization or post-curing.

Results and images in Figure 2 already showed that the 3D printed structures become soft and pliable post heating, but maintain their structural integrity, i.e., their shape. To verify the material's stability during multiple usage cycles (particularly to check if any phase change material leakage occurs during repeated melting), we conducted 30 cycles of DSC testing on a printed PA 60 sample. By monitoring any shifts in the endothermic and exothermic peaks during DSC cycling, one can determine whether PCM leakage occurs.[26,27] Here, PA 60 was selected for thermal cycling assessment as it contains the highest paraffin content among all formulations, thus representing the most susceptible composition to potential leakage. The

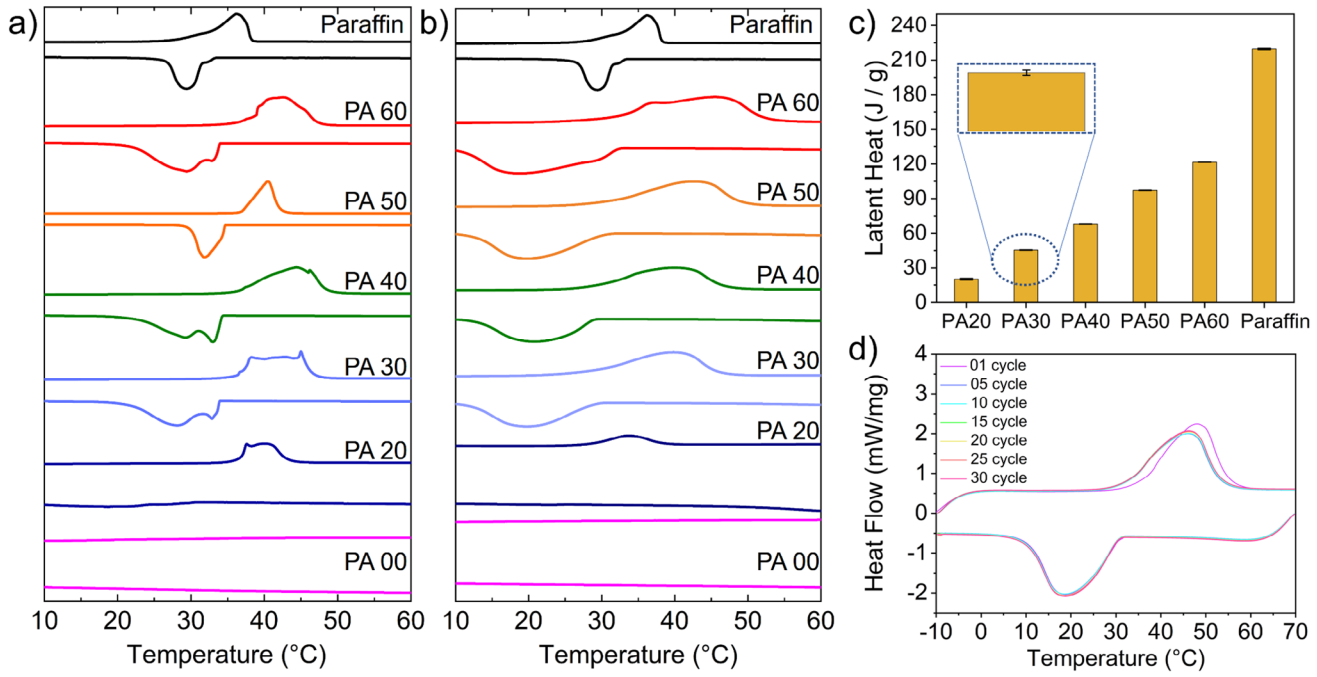

Figure 5. Thermal characterization of PA 00–PA 60 in increments of 10 wt.% compared with pure paraffin. a) DSC curves of the cured resins compared with pure paraffin. b) DSC curves of DLP printed parts of PA 00–PA 60 compared with pure paraffin. c) Latent heat during phase transition as a function of the total amount of PCM in the resins. Error bars were calculated from four repeated experiments. d) Thermal cycling (up to 30 full cycles) of a cured sample of PA 50. As can be seen, only slight variations in heat flow can be observed.

experimental results are shown in Figure 5d., the DSC peak shift from the first cycle and is stable from the 2nd to the 30th cycle, one can expect low leakage in paraffin of the sample, indicating the reliability of the shape-stabilized paraffin. To further evaluate the thermal stability of our materials, we conducted analysis including thermogravimetric analysis (TGA), high-temperature DSC measurements, and visual inspection after thermal treatment (Figure S11, Supporting Information), which confirmed the material stability up to 150 °C while maintaining its phase change properties.

Thermal conductivity is a key indicator of PCM's sensitivity to temperature changes, determining how efficiently the PCM will absorb or release heat to the environment. This property is important in thermo-responsive materials such as our Paraffin Photoresin, as it directly influences the materials response time to temperature variations. In order to study the effect of the presence of polymers, the thermal conductivity of the printed sample was measured (see Table 1 alongside the DSC results). The pure paraffin used in this study has a thermal conductivity of 0.21 W · mK^{-1}. The printed PA 20 to PA 60 samples exhibited thermal conductivities ranging from 0.04 to 0.12 W · mK^{-1} due to the incorporation of polymer network. This combination of reduced thermal conductivity and high latent heat capacity makes this material promising for thermal protection applications.[28,29] For example, recent work has demonstrated that PCMs with lower thermal conductivity can effectively delay heat transfer and provide better temperature control in applications such as wearable electronics thermal management.[30] Furthermore, combined with

Table 1. Thermal properties derived from DSC measurements for cured printed parts PA 20 to PA 60 in increments of 10 wt.%. We derived the melting range, i.e., the range of the phase transition, ΔH_m (latent heat of melting) and ΔH_c (latent head of crystallization) as well as the measured thermal conductivity.

Sample	Melting Range [°C]			ΔH_m [J · g^{-1}]	ΔH_c [J · g^{-1}]	Thermal Conductivity [W · mK^{-1}]
	T_i	T_m	T_f			
PA 20	27.7	33.9	42.2	20.25 ± 0.77	–	0.10
PA 30	27.2	39.8	46.6	45.46 ± 0.26	−32.33 ± 0.81	0.12
PA 40	26.8	39.9	49.7	67.82 ± 0.15	−63.62 ± 0.19	0.11
PA 50	25.9	42.4	52.7	97.22 ± 0.20	−92.90 ± 0.29	0.09
PA 60	25.6	45.4	54.9	121.55 ± 0.12	−117.45 ± 0.33	0.07
Paraffin	26.1	36.5	38.9	219.55 ± 0.63	−219.3 ± 0.08	0.21

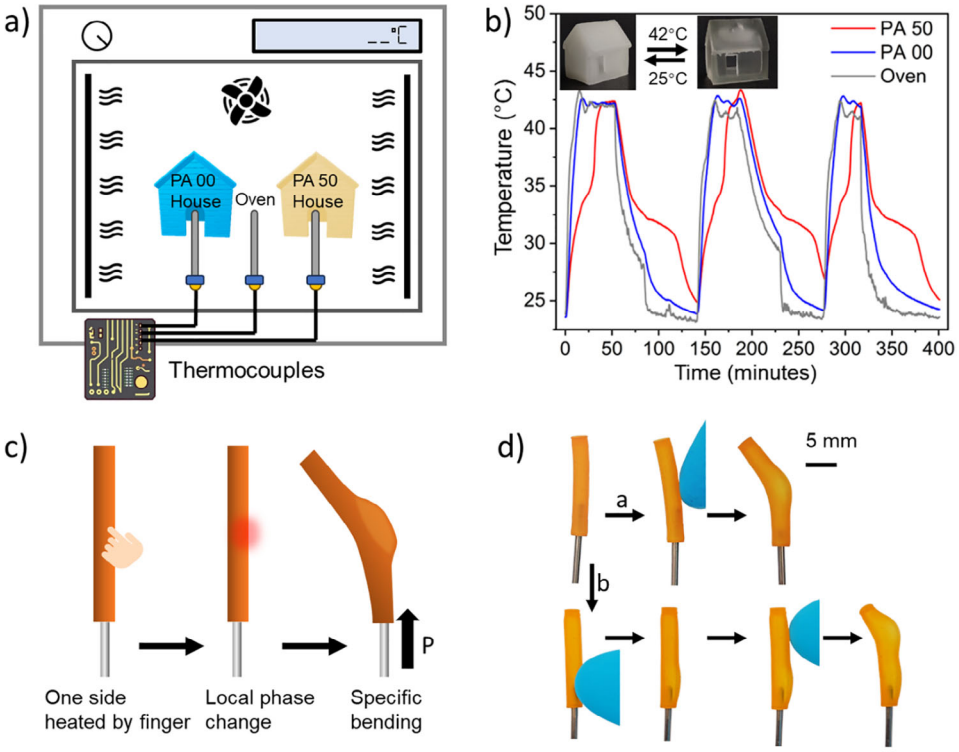

Figure 6. Application examples of 3D printed Paraffin Photoresin. a) Schematic of the experimental setup for thermal management application: In a drying oven small 3D printed houses made from PA 00 and PA 50, respectively, were placed with thermocouples monitoring the temperature inside the structures. A thermocouple was placed outside as a reference. b) Temperature profiles as a function of time for three thermal cycles from the three thermocouples. As can be seen, the temperature inside the structure made from PA 50 is delayed showing the thermal buffering capabilities. c) The working principle of the column printed based on PA 30 as a body temperature responsive pneumatic actuator. The modulus change caused by the phase change of PA 30 caused by body temperature will allow the column to produce specific bending when pressurized. d) Potential mode of movements of this actuator.

the advantage of 3D printing enabling complex geometries, the 3D printable Paraffin Photoresin offers a cost-effective and versatile solution for thermal protection applications where delayed heat transfer is desired. On the other hand, if the thermal conductivity needs to be improved, the material could be further optimized through the addition of conductive fillers or structural design for specific application requirements.

The DLP 3D printing technology demonstrates significant potential for fabricating thermal management microstructures, as it enables rapid production of PCM composites with high resolution and dimensional accuracy. To validate the thermal regulation performance of these printed composites, we designed a comparative experiment using two identical house-scale models made of PA 50 and PA 00. The experimental setup (**Figure 6a**) features these small houses placed inside a temperature-controlled drying oven with circulating hot air to ensure uniform temperature distribution. Three thermocouples were positioned to monitor temperature variations: One inside each house model and the third in the oven chamber as a reference. While the test is initialized from room temperature, i.e., 25 °C, the target temperature was set to 42 °C, which is above the melting temperature range of paraffin, to ensure complete phase transition during the heating process. Once the internal temperatures of both houses reached 42 °C, the system was allowed to cool passively to 25 °C, with the oven door closed, simulating a real-world thermal management scenario. This setup enables direct comparison of the thermal response characteristics between PA 50 and PA 00 under identical heating and cooling conditions.

Results of temperature as function of time is shown in Figure 6b demonstrating that, while heating up, the thermocouple inside the printed structure has a significantly delayed temperature increase compared to the reference as well as the thermocouple in the structures made from PA 00. During the cooling process, both structures as well as the reference have similar initial profiles of temperature drop at the start of the experiment with the thermocouple in the structure printed from PA 50 significantly slows down near the phase change temperature. This is due to the latent heat storage and release characteristics of the paraffin. The PA 50 structure maintained a 11 °C temperature difference and effectively modulated the variation in temperature. This cycle is repeated a total of three times finding close-to-identical results.

In addition to thermal management, 3D printed our Paraffin Photoresin has significant potential for the fabrication of pneumatic soft actuators with the potential to respond to, e.g., touch. This effect is based on their phase transition temperature close to the human body temperature enabling temperature-responsive actuation capabilities. Figure 6c illustrates the

fundamental mechanism of such an actuator, whose simplest form is a closed flexible cylinder. At room temperature (i.e., below the phase transition point of PAs) applying pressure to the inside will cause it to expand uniformly in all directions. However, localized contact with a warm object, such as a finger, induces a phase transition in the contact region, enabling a responsive interaction between the actuator and user.

To demonstrate this behavior, such a cylinder-shaped actuator was printed with PAs30. Initial pressurization to 50 mbar induced no observable deformation. When the actuator was heated locally by contact with a finger a temperature-responsive actuation was triggered resulting in structural bending of the actuator in the direction opposite of the point of contact. Among all PA materials, PA30 showed the most sensitive to finger touching, and its bending modes were position-dependent (on the placement of warm contact) as shown in Figure 6d and Video S3 (Supporting Information). These results illustrate temperature responsiveness of the material, similar to our programmable actuators previously reported.[31] These findings suggest promising applications in human-interactive soft robotics and actuator and sensor systems, since the temperature response range of the PA series coincides with human body temperature.

3. Conclusion

This study demonstrates a low-cost "core-shell free" method for preparing shape-stabilized paraffin using DLP-based 3D printing via a custom-developed Paraffin Photoresin. This study presents a significant advancement in PCM fabrication by combining low-cost materials with high-precision DLP printing to achieve relative higher stretchability while maintaining substantial latent heat capacity. By combining paraffin with acrylate-based monomer and crosslinkers, we were able to successfully print complex structures. The resulting elastomeric paraffin composite containing up to 60 wt.% of paraffin shows an effective thermal responsiveness without leakage of the paraffin. Our analysis confirmed that the paraffin is well incorporated within the polymeric matrix. Thermal and mechanical analysis verified that these shape-stabilized paraffin components function effectively as a PCM component with a latent heat capacity of 128 Jg^{-1}, while also retaining elasticity and stretchability above the melting point. DSC cycling tests confirmed its thermal stability without paraffin leakage for (at least) 30 thermal cycles. These findings confirm the reliability and practicality of this paraffin resin as a novel material for functional 3D printed components paving the way for applications in thermal management, temperature-responsive actuators as well as programmable functional metamaterials based on paraffin actuators. Considering that this material system is based on commercially available, low-cost components and standard DLP printing conditions, we envision its potential for industrial-scale applications, which will be systematically investigated in future studies.

4. Experimental Section

Materials: Genomoer 4230 (AUA) was kindly provided by Rahn AG, Germany. CrodaTherm 37 was provided by Croda Inc., Germany. Tinuvin-326 was kindly provided by BASF, Germany. IA and TPO were purchased from Sigma–Aldrich, Germany and used as provided.

Preparation of Paraffin Photoresins: To prepare resins for DLP 3D printing, the components were mixed (see Table S2, Supporting Information) by sonication at 40 °C in an ultrasonic bath for 30 min, after which colorless liquids were obtained.

3D Printing: All prints were carried out on the vat-based DLP printer Asiga Pico 2 (Asiga, Germany) with a lateral resolution of 50 µm. The printer is equipped with a temperature sensing module to maintain a stable printing temperature of 40 °C, which requires setting the internal heating system to 50 °C in the Asiga System. The printing parameters are listed in Table S3 (Supporting Information). The dosage calibration step with the following procedure was performed to find the right printing parameters. The freshly prepared resin was dropped onto a glass slide until it spread completely. Light spots (d = 3 mm) with the same energy density as during printing were exposed for different amounts time (from 4 to 15 s). After exposure, the uncured resin was removed, and the glass slides were washed with 2-propanol and dried in nitrogen gas. The height of the spots was measured, and the corresponding energy dosage was calculated according to the equation $E_{exposure} = I_{light} \bullet t_{exposure}$, in which the light intensity was detected to be 6.2 mW cm^{-2}. To determine the required exposure for the given layer thickness, the layer thickness was plotted against the exposure energy and an adjusted exposure time suitable for 50 µm was chosen for all prints. After the successful printing, the components were flushed with 2-propanol and dried with nitrogen gas.

House Thermal Test: The thermal behavior of printed samples was evaluated using temperature-controlled drying oven (Memmert model 30–1060) equipped with an electric fan for air circulation. Temperature measurements were conducted using three K-type thermocouples connected to a digital thermometer (Testo-735). Two house-scale models were printed using PA 50 (Paraffin Photoresin) and PA 00 (pure resin) respectively. The thermocouples were placed inside each house model and in the oven chamber. The system was heated from 25 to 42 °C and then allowed to cool naturally with the oven door closed.

Characterization—SEM: The SEM images were taken with a FEI Scios 2 Hivac system (Thermo Fischer, USA) at different micrometer scales. Thin slices were carefully extracted from the sample surface for measurement.

Characterization—Micro-Computed Tomography (µ-CT): For internal microstructure analysis of the printed samples µ-CT images were obtained using a µCT (Skyscan 1272, Bruker, Kontich, Belgium). The Skyscan 1272 mCT software (version 1.1.10), CTvox (Bruker) was used for reconstruction. Ilastik and Avizo software was used for segmentation.

Characterization—XRD and In Situ WAXS: XRD measurements were obtained using a D8 Discover diffractometer (BRUKER AXS, USA) at room temperature with a LynxEye XE-T-Detector under Cu/K radiation. The measurement was done from $2\theta = 2°$ to 50° with 0.05° incremental steps.

In situ WAXS was conducted with a Metal Jet D2 X-ray source (Excillum, Sweden) with a liquid anode composed of Ga-In-Sn alloy liquid, the electrons were accelerated under 70 kV, and a Montel-optic (AXO, Germany) was used to focus and select the Ga K_α line. A Pilatus 1 M detector (Dectris, Switzerland) acquired the angle-dispersive 2D diffraction patterns, which were transformed, integrated over the angular range and background corrected.

Characterization—DSC: The DSC was performed using a NETZSCH DSC 204F1 Phoenix with an accuracy of ±0.1 K in dynamic mode of heating with 1 K/min and 10 K/min heating rates. The measurements were obtained from −20 to 100 °C in a standard Al 25 µL crucible with pierced lid under nitrogen purging with a flow rate of 20 mL min^{-1} and a pressure of 1.6 psi. The weight of the sample was inconsistent for each sample due to the small sample size required and the difficulty in cutting the exact size from such light materials. However, the mass of the samples tested was between 10 and 20 mg. The transition temperatures, latent heat and thermal stability of the samples were analyzed with the Proteus software from Netzsch.

Characterization—Thermal Conductivity: Thermal conductivity measurements were performed using the Transient Hot Bridge THB100 setup (LINSEIS GmbH, Selb, DE) with the THB A metal sensor at room temperature. The uncertainty of the thermal conductivity measurement specified by the manufacturer is 0.01 $W \cdot mK^{-1}$. For precise measurement, the appropriate measurement current (50 mA) and time were selected by

calibrating the sensor with known materials. All data were collected and analyzed using the LINSEIS platinum software.

Characterization—Tensile Test: Strain-stress tests were performed using an Inspekt Table 5kN universal tensile testing machine (Hegewald & Peschke Meß- und Prüftechnik GmbH, Germany) with a 100 N load cell. The tested parts were printed 10 mm × 4 mm × 1 mm dogbone-shaped components. The tensile tests for calculating Young's Modulus and yield stretchability were performed using a strain rate of 50 mm min^{-1} in a thermostatic box at 42 °C. Tensile tests were performed three times for each sample to calculate the average yield strain and Young's modulus. The Young's modulus was obtained from the slope of the stress–strain curve within 10% strain.

Characterization—In Situ UV–vis Spectroscopy: In situ UV–vis spectra were recorded on an Ocean FX spectrophotometer, the collector automatically collected the UV–vis spectrum in the wavelength range of 200–900 nm every 100 s, and the collection time window was set to 10 ms. A PA 60 sheet sample with a thickness of 1 mm and a length and width of 10 mm was placed between the light source and the receiver and maintained at a constant temperature of 25 °C.

Characterization—Rheology Measurements: The viscosity of the resin samples was measured on an MCR 302e rheometer with a MESSPLATTE PP50 sensor. The resin was preheated to 65 °C and cooled to 15 °C within 300 s, using a speed of 10 rad s^{-1} and an amplitude of 1% to measure the viscosity of the sample.

Characterization—Length Retention Measurements: The dimensional stability of printed samples during phase transition was evaluated through optic microscopic measurements. Specimens with dimensions of 10 mm × 10 mm × 1 mm were printed using different formulations (PA 20 – PA 60). The length of each specimen was measured at 42 and 15° C under microscopic observation. The length retention ratio (R_r) was calculated using the following equation:

$$R_r = \left(1 - \frac{L_{42} - L_{15}}{L_{42}}\right) \times 100\% \quad (1)$$

where L_{42} and L_{15} represent the measured length at 42 and 15 °C, respectively. Each measurement was repeated three times to ensure reliability.

Characterization—Swelling Test: The swelling behavior of pure polymer network (PA 00) in liquid paraffin was investigated at 65 °C. Printed PA 00 samples were weighed and then immersed in liquid paraffin. The samples were removed at predetermined time intervals, quickly wiped with filter paper to remove excess surface paraffin, and weighed. The swelling ratio (S_r) was calculated according to:

$$S_r = \frac{W_t - W_0}{W_0} \times 100\% \quad (2)$$

where W_t and W_0 are the weights of the sample at time t and initial state, respectively.

Characterization—TGA: The TGA experiment is conducted with a STA409C system from Netzsch Gerätebau GmbH.

Supporting Information

Supporting Information is available from the Wiley Online Library or from the author.

Acknowledgements

S.K.S. and Q.S. contributed equally to this work as co-first authors. Funded by the Deutsche Forschungsgemeinschaft (DFG, German Research Foundation) under Germany's Excellence Strategy – EXC-2193/1 – 390951807. The authors would like to thank Dr. Thilo Ludwig and Dr. Yi Thomann for their assistance with XRD and micro-CT experiments respectively. The authors thank Rahn AG for kindly providing the Genomer resin material.

Conflict of Interest

The authors declare no conflict of interest.

Data Availability Statement

The data that support the findings of this study are available from the corresponding author upon reasonable request.

Keywords

digital light processing, paraffin, phase change material, thermal management, thermal storage

Received: March 23, 2025
Published online:

[1] F. Castro, K. K. Westbrook, K. N. Long, R. Shandas, H. J. Qi, *Mech. Time-Depend. Mater.* **2010**, *14*, 219.
[2] P. Wei, C. E. Cipriani, E. B. Pentzer, *Matter* **2021**, *4*, 1975.
[3] D. N. Nkwetta, F. Haghighat, *Sustainable Cities. Soc.* **2014**, *10*, 87.
[4] S. Bista, S. E. Hosseini, E. Owens, G. Phillips, *Appl. Therm. Eng.* **2018**, *142*, 723.
[5] J. Li, P. Xue, H. He, W. Ding, J. Han, *Energy Build.* **2009**, *41*, 871.
[6] J. Solomon, V. Kugarajah, P. Ganesan, S. Dharmalingam, *J. Environ. Chem. Eng.* **2022**, *10*, 107057.
[7] Z. Khan, Z. Khan, A. Ghafoor, *Energy Convers. Manage.* **2016**, *115*, 132.
[8] X. Zuo, J. Li, X. Zhao, H. Yang, D. Chen, *Renewable Energy* **2020**, *152*, 579.
[9] Q. Al-Yasiri, M. Szabó, *Renewable. Energy Environ. Sustainability.* **2021**, *6*, 38.
[10] H. Johra, P. Heiselberg, *Renewable Sustainable Energy Rev.* **2017**, *69*, 19.
[11] C. A. Saleel, M. A. Mujeebu, S. Algarni, *J. Therm. Anal. Calorim.* **2019**, *136*, 629.
[12] H. Mahmud, M. Islam, M. E. J. Khan, D. H. Ahmed, *Energy. Ecol. Environ.* **2023**, *8*, 241.
[13] M. Mu, S. Zhang, S. Yang, Y. Wang, *J. Energy Storage* **2022**, *49*, 104100.
[14] X. Wang, G. Li, G. Hong, Q. Guo, X. Zhang, *ACS Appl. Mater. Interfaces.* **2017**, *9*, 41323.
[15] E. J. Tremblay, D. Loterie, C. Moser, *Opt. Express* **2012**, *20*, A964.
[16] N. S. Dhaidan, J. M. Khodadadi, T. A. Al-Hattab, S. M. Al-Mashat, *Int. J. Heat Mass Transfer.* **2013**, *66*, 672.
[17] X. Py, R. Olives, S. Mauran, *Int. J. Heat Mass Transfer.* **2001**, *44*, 2727.
[18] S. Peng, A. Fuchs, R. A. Wirtz, *J. Appl. Polym. Sci.* **2004**, *93*, 1240.
[19] Y. Er, O. Güler, G. Hekimoğlu, M. Nodehi, A. Ustaoğlu, A. Sarı, O. Gencel, T. Ozbakkaloglu, *J. Energy Storage.* **2023**, *73*, 109124.
[20] M. Malik, I. Dincer, M. A. Rosen, *Int. J. Energy Res.* **2016**, *40*, 1011.
[21] T. D. Ngo, A. Kashani, G. Imbalzano, K. T. Q. Nguyen, D. Hui, *Composites, Part B* **2018**, *143*, 172.
[22] D. Han, Z. Lu, Z. Lu, S. A. Chester, H. Lee, *Sci. Rep.* **2018**, *8*, 1963.
[23] J. Ma, T. Ma, J. Cheng, J. Zhang, *Energy Storage Mater.* **2021**, *39*, 294.
[24] B. Li, T. Liu, L. Hu, Y. Wang, L. Gao, *ACS Sustainable Chem. Eng.* **2013**, *1*, 374.
[25] M. Boin, D. Apel, F. García-Moreno, C. Genzel, P. Kamm, M. Klaus, R. Mainz, G. Wagener, R. Wimpory, in Proc. FLS2023, JACoW Pulishing, Luzern, Switzerland, **2023**, 5.
[26] X. Y. D. Soo, J. K. Muiruri, J. C. C. Yeo, Z. M. Png, A. Sng, H. Xie, R. Ji, S. Wang, H. Liu, J. Xu, X. J. Loh, Q. Yan, Z. Li, Q. Zhu, *SmartMat* **2023**, *4*, 1188.

[27] Y. Li, W. C. Tie, Q. Z. Zhu, Z. Z. Qiu, *Int. J. Thermophys.* **2021**, *42*, 155.
[28] P. Liu, H. Gao, X. Chen, D. Chen, J. Lv, M. Han, P. Cheng, G. Wang, *Composites, Part B* **2020**, *195*, 108072.
[29] K. Yuan, J. Shi, W. Aftab, M. Qin, A. Usman, F. Zhou, Y. Lv, S. Gao, R. Zou, *Adv. Funct. Mater.* **2020**, *30*, 1904228.
[30] Y. Shi, C. Wang, Y. Yin, Y. Li, Y. Xing, J. Song, *Adv. Funct. Mater.* **2019**, *29*, 1905470.
[31] Q. Song, Y. Chen, V. Slesarenko, P. Zhu, A. Hamza, P. Hou, D. Helmer, F. Kotz-Helmer, B. E. Rapp, *ACS Appl. Mater. Interfaces.* **2023**, *15*, 40923.